# Poisson-Schrödinger simulation and analytical modeling of inversion charge in FDSOI MOSFET down to 0 K – Towards compact modeling for cryo CMOS application

M. Aouad, T. Poiroux, S. Martinie, F. Triozon, M. Vinet, Gérard Ghibaudo

Version of Record: https://www.sciencedirect.com/science/article/pii/S0038110121001696
Manuscript_e6a0becc23594bc7557db0345bf8cf7a

# Poisson-Schrödinger simulation and analytical modeling of inversion charge in FDSOI MOSFET down to 0K – Towards compact modeling for cryo CMOS application

M. Aouad[1], T. Poiroux[1], S. Martinie[1], F. Triozon[1], M. Vinet[1], G. Ghibaudo[2]

1) CEA-LETI, Univ. Grenoble Alpes, Minatec, 38054 Grenoble, France, 2) IMEP-LAHC, Univ. Grenoble Alpes, Minatec, 38016 Grenoble, France. e-mail address: mohamed.aouad@cea.fr

***Abstract*—Poisson-Schrödinger (PS) simulations and an analytical charge model for a back biased FDSOI structure operated at deep cryogenic temperatures have been developed. PS simulations have been conducted down to 0K, where metallic statistics applies, by replacing the $F_0$ Fermi integral by a Heaviside function. Considering, as a first approximation, two separated channels for front and back interface, a set of implicit equations has been established based on a single subband scheme within the Airy approach, providing a good description of surface potential, inversion charge and capacitance characteristics of FDSOI structures operated at very low temperature and for various back biases and silicon thicknesses. This analytical charge model is a first step towards a compact model of FDSOI MOSFET for circuit design at cryogenic condition.**

***Keywords*—FDSOI, cryo-CMOS, Poisson-Schrödinger, compact model, Airy approach, Fermi-Dirac statistics.**

## I. Introduction

Research on cryogenic electronics has started decades ago [1] with application in the spatial field. Nowadays, the emergence of quantum computing restores the interest for cryogenic applications. Indeed, in order to control the Qubit (which ideally operates around 0K), a nearby electronics operating at deep cryogenic temperatures (between 0 and 4 K) is mandatory [2]. Early demonstration of quantum computers have illustrated their potential when several qubits are operating, and cryo-electronics is necessary to assure the control and read-out of such a large number of qubits. FDSOI cryo-CMOS is a promising candidate to this end due to its superior electrostatic control, no channel doping needed, higher performance and low power consumption.

It should be noted that many works have been done before on Poisson-Schrodinger simulation in bulk or FDSOI MOSFETs at room or low temperatures [3-7] but not down to very low temperatures (<2K). Besides, CEA-LETI has developed a physics-based compact model dedicated to ultrathin body and buried oxide fully depleted silicon-on-insulator (UTBB) transistor called L-UTSOI [8]. However, this model has not been conceived for deep cryogenic temperature operation. In this paper, we demonstrate for the first time Poisson-Schrodinger simulations of carrier charge in FDSOI structure down to 0K. Then, we propose the first charge numerical model for FDSOI devices with back biasing operation at deep cryogenic conditions. We also detail the mathematical developments necessary to solve analytically the two equations that couples the front and back channels, starting from initial guesses, then converging to the exact solutions owing to a number of error correction steps.

## II. Simulation methodology

Our Poisson-Schrödinger (PS) solver is based on a Python program solving self-consistently the Schrodinger and Poisson equations recalled below:

$$H(\psi_{ij}) = E_{ij}.\psi_{ij} \quad (1)$$

$$\nabla(\varepsilon_r \nabla V) = -\frac{q.n(x)}{\varepsilon_0} \quad (2)$$

With H the Hamiltonian, $E_{ij}$ the i[th] subband energy level of valley j, $\psi_{ij}$ the corresponding electron wave function, $\varepsilon_0$ and $\varepsilon_r$ the vacuum and relative silicon permittivity.

Once the electrical potential V, the subband energies $E_{ij}$ and the wave functions $\psi_{ij}$ are computed in a FDSOI structure, the electron density is obtained by summing the different valleys and subband contributions as:

$$n(x) = \sum_{j=1}^{2} \sum_{i=1}^{imax} g_j A_{2dj} kT.\psi_{i,j}^2(x).F_0\left(\frac{E_f - E_{i,j}}{kT}\right) \quad (3)$$

with kT the thermal energy, $F_0$ the zero-order Fermi-Dirac integral function, $E_f$ the Fermi level, $g_j$ the valley degeneracy and $A_{2dj}$ the 2D density of states for valley j.

In order to simulate the PS equations down to very low temperature (1K), special truncation care has been taken to avoid numerical overload in the $F_0$ Fermi integral function accounting for Fermi-Dirac statistics. PS simulations were even made possible at the 0K limit by replacing the $F_0$ Fermi-Dirac integral function by a Heaviside function, emulating the fully degenerate metallic statistics.

# III. Results and discussion

## A. *Poisson-Schrödinger simulation*

Typical FDSOI structure used for PS simulation is shown in Fig. 1, illustrating the band diagram across the stack and the electron density profile in the channel obtained from PS solution at T=4K for a given bias condition. Without loss of generality, midgap gates are considered in this study.

Figure 2 shows the variations of the inversion charge $Q_i$ in the Si channel as a function of front gate voltage $V_g$ with a back bias $V_b$=+3V, obtained from PS simulations for various temperatures T=0-60K. Note the strong decrease of the subthreshold swing with temperature lowering, becoming ideally null at T=0K, which is an appealing consequence of transistors functioning at such low temperatures.

Figure 3 better illustrates the channel inversion charge control by field effect via the variations of the gate-to-channel capacitance $C_{gc}(V_g)=dQ_i/dV_g$ with front gate voltage for various back gate bias, revealing the early onset of back inversion channel followed by the front channel opening for $V_b$=+3V. This feature of $C_{gc}(V_g)$ curve clearly reveals the through-the-silicon coupling between the front gate and the back channel inversion layer with a lower capacitance on the first plateau.

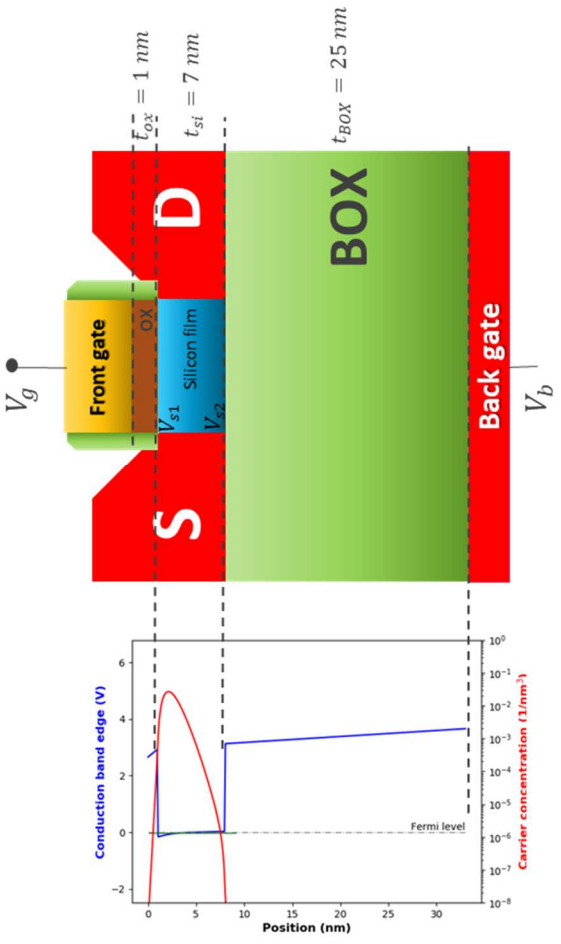


**Fig. 1.** Typical scheme, band diagram and electron distribution from PS simulation for a FDSOI structure (Vg=1V, tox=1nm, tbox=25nm, tsi=7nm,Vb=0V, T=4K).

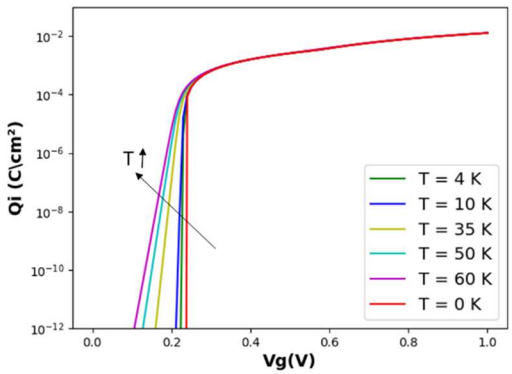


**Fig. 2.** $Q_i(V_g)$ for different temperatures (tox=1nm, $t_{box}$=25nm, $t_{si}$=7nm, $V_b$=+3V).

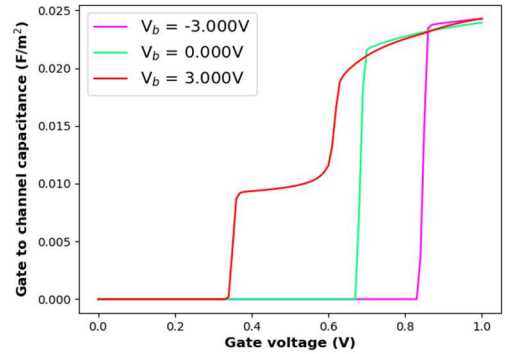


**Fig. 3.** Cgc(Vg) curves for different back bias (tox=1nm, tbox=25nm, tsi=10nm, T=4K).

The influence of temperature on the $C_{gc}(V_g)$ curves is displayed in Fig. 4, clearly showing the rounding of the curves with temperature increase above T=10K. Note that these simulation results well agree with experimental ones shown in [7].

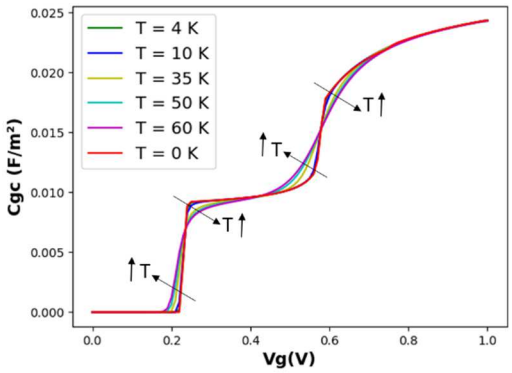


**Fig. 4.** Cgc(Vg) curves for different temperatures (tox=1nm, tbox=25nm, tsi=10nm,Vb=+3V).

Moreover, in Fig. 5 is reported the impact of silicon channel thickness on the $C_{gc}(V_g)$ characteristics at T=4K and $V_b$=+3V, demonstrating a delayed and stronger through-the-silicon back channel coupling as the silicon film thickness is

reduced. Note also the larger capacitance shoulder effect before front channel opening for $t_{si}$=7nm, which can be explained by the higher carrier profile overlap between the back and front interface electron distributions as $t_{si}$ is reduced (see Figure 6). Instead, for larger $t_{si}$ values, the overlap is decreased, so that front and back channels are better separated.

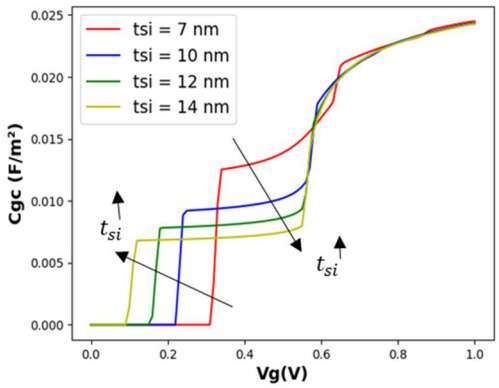


**Fig. 5.** $C_{gc}(V_g)$ curves for different channel thickness ($t_{ox}$=1nm, $t_{box}$=25nm, T=4K, $V_b$=+3V).

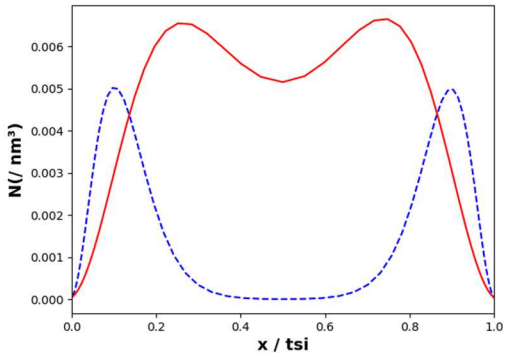


**Fig. 6.** Electron distrubution in the channel ($t_{ox}$=1nm, $t_{box}$=25nm, $t_{si}$=7nm for red line and $t_{si}$ = 16 nm for blue dashed line, T=4K, $V_g$=0.73V, $V_b$=+3V).

## *B. Airy function based Numerical model*

Based on the PS simulation results, a numerical model has been developed considering that front and back channel charges can be calculated separately at each interface on a single subband, whose energy level is given by the triangular potential well approximation within Airy's function approach [10]. The coupling is achieved by the mean of the silicon channel capacitance $C_{si}$ and the charge sheet approximation [11] along with Fermi-Dirac statistics chosen to describe the system.

In this context, the charge conservation equations at front and back interfaces are written as:

$$V_g = V_{fb} + V_{s1} + \frac{qN_{inv1}}{C_{ox}} + \frac{C_{si}\cdot(V_{s1}-\Delta V(F_1)-V_{s2}+\Delta V(F_2))}{C_{ox}} \quad (4)$$

$$V_b = V_{fb} + V_{s2} + \frac{qN_{inv2}}{C_{box}} + \frac{C_{si}\cdot(V_{s2}-\Delta V(F_2)-V_{s1}+\Delta V(F_1))}{C_{box}} \quad (5)$$

With front and back interface 2D carrier density given by,

$$N_{inv1,2} = A_{2d}.k.T.F_0\left[\frac{V_{s1,2}-V_0-\Delta V(F_{1,2})}{kT}\right] \quad (6)$$

Where $V_{s1}$ ($V_{s2}$) is the front (back) interface surface potential, $C_{ox}$ ($C_{box}$) the front (back) oxide capacitance, $C_{si}$ the silicon film capacitance. The front and back electric fields in the silicon film are given by:

$$F_1 = (V_g - V_{s1} - V_{fb})/3t_{ox} \quad (7)$$

$$F_2 = (V_b - V_{s2} - V_{fb})/3t_{box} \quad (8)$$

with Airy's subband potential shift $\Delta V(F) = K.F^{2/3}$ with K=1.488x10$^{-5}$V$^{1/3}$cm$^{2/3}$, the factor 3 corresponds to $\varepsilon_{si}/\varepsilon_{ox}$ , with $\varepsilon_{si}$ and $\varepsilon_{ox}$ the permittivities of the silicon film and the oxides respectively. For numerical purpose, we rewrite the quantum shift $\Delta V(F) = K.(F^2)^{1/3}$, which is the same but with an absolute value of the field. The quantum shift in the negative field region assumes the existence of a subband well above the conduction band. This fictive subband is actually not filled with electrons and has no impact on the total charge. It is just kept for computation reason and ensure a good description of the function in all regimes. Introducing the $\Delta V(F_{1,2})$ expressions to the coupling term will allow a more accurate description and add more stability to the model around the zero electric field zone. Furthermore, this attribution allows a good description of the $C_{gc}$ curves especially in the coupling part that appears during the opening of the front channel (see Figures 10 & 11).

Typical $Q_i(V_g)$, $V_s(V_g)$ and $C_{gc}(V_g)$ characteristics obtained by this simple Airy-based numerical model are compared in Figs 7-11 to the PS simulation results, showing an overall good agreement between them, especially for not too small silicon thickness where wave function overlap between front and back interface is not important. The results point out the main set of implicit equations to be solved for cryogenic analytical model.

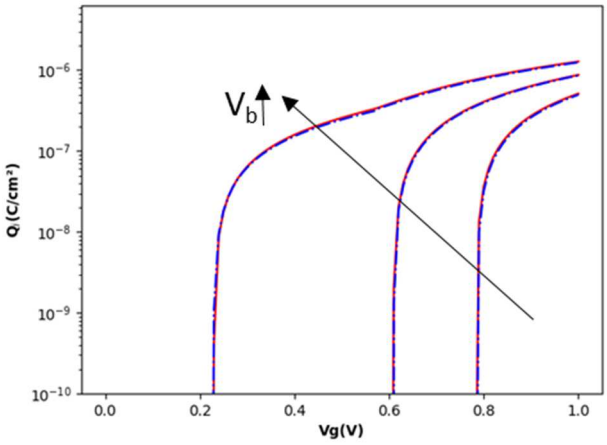


**Fig. 7.** Qi(Vg) curves obtained from PS simulations (solid lines) and numerical modeling (dashed lines) for various Vb=-3, 0, +3V (T=4K, tox=1nm, tbox=25nm, tsi=10nm).

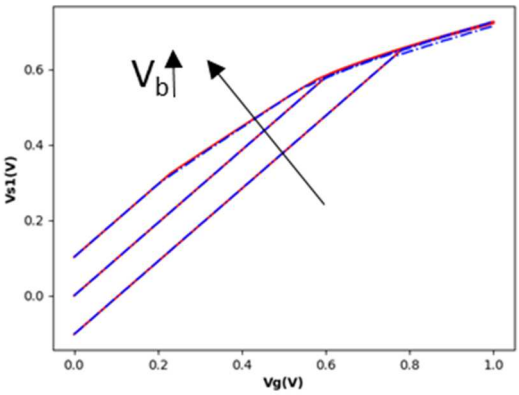


**Fig. 8**. Comparison of front surface potentials $V_{s1}(V_g)$ curves as obtained from PS simulations (solid lines) and numerical modeling (dashed lines) for various $V_b$=-3, 0, +3V (T=4K, $t_{ox}$=1nm, $t_{box}$=25nm, $t_{si}$=10nm).

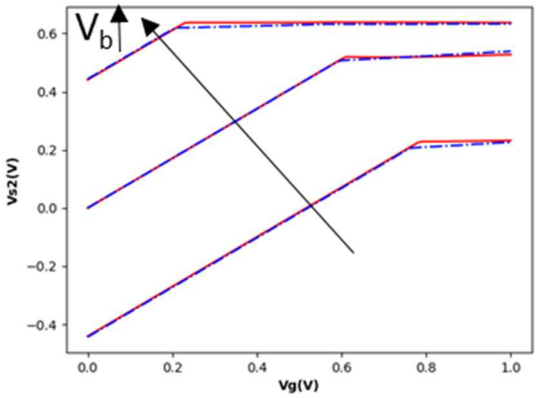


**Fig. 9**. Comparison of back surface potential $V_{s2}(V_g)$ curves as obtained from PS simulations (solid lines) and numerical modeling (dashed lines) for various $V_b$=-3, 0, +3V (T=4K, $t_{ox}$=1nm, $t_{box}$=25nm, $t_{si}$=10nm).

In Fig. 12 are also reported the variation with gate voltage of the fraction of inversion charge in the back channel and in the front channel, as obtained from PS simulations and numerical model. Note the very good agreement between both approaches, further underlying the pertinence of the numerical modeling.

It should be noted that contrary to literature [12], the use of Boltzmann statistics may not be sufficient to address charge modeling at cryogenic temperatures (in particular for FDSOI application).

These different results point out the main set of implicit equations mandatory to solve explicitly for cryogenic analytical model.

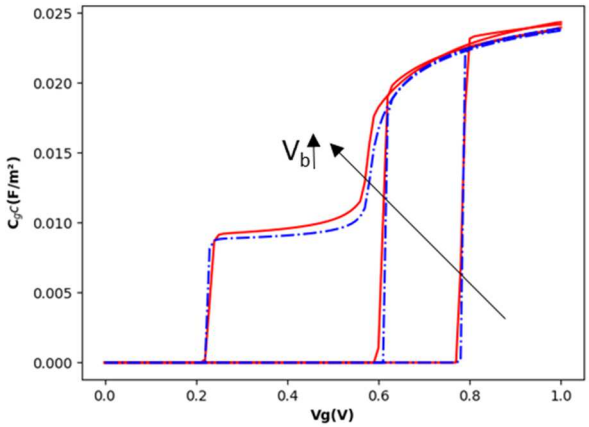


**Fig. 10.** $C_{gc}(V_g)$ curves obtained from PS simulations (solid lines) and numerical modeling (dashed lines) for various parameters $V_b$=-3, 0, +3V (T=4K, $t_{ox}$=1nm, $t_{box}$=25nm, $t_{si}$=10nm).

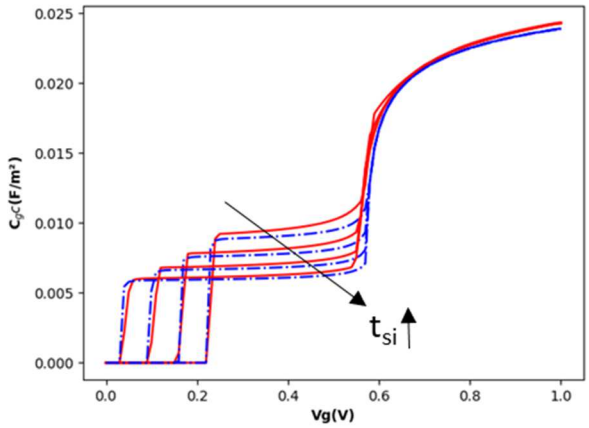


**Fig. 11.** $C_{gc}(V_g)$ curves obtained from PS simulations (solid lines) and numerical modeling (dashed lines) : for various $t_{si}$=10, 12, 14, 16 nm (T=4K, $t_{ox}$=1nm, $t_{box}$=25nm, $V_b$=+3V).

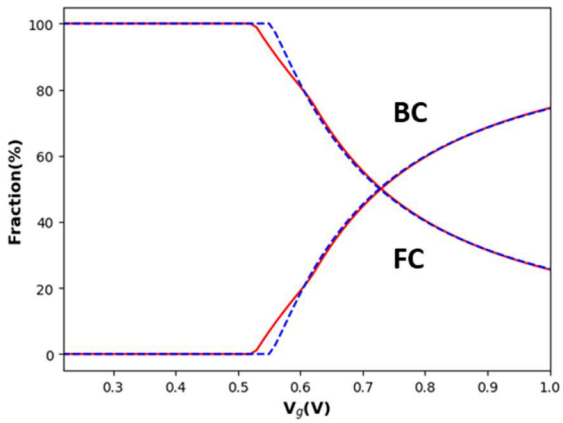


**Fig. 12.** Variation of fraction of inversion charge in back channel (BC) and front channel (FC) with front gate voltage as obtained from PS simulations (solid lines) and numerical model (dashed lines) curves (T=4K, $t_{ox}$=1nm, $t_{si}$=10nm, $t_{box}$=25nm, $V_b$=+3V).

## C. *Airy function based Analytical model*

Here we detail the steps necessary to develop a suitable analytical formulation needed for compact modelling. To this end, we start from our system of equations (4-5) without considering the quantum shift, and we write both in the weak and strong inversion configurations (Equations 9 to 12). Using Fermi-Dirac statistics inherent to cryogenic consideration have the advantage of the explicit formulation in both strong and weak inversions.

We consider four cases: The case where both interfaces are in weak inversion or in strong inversion, the case where front interface is strongly inverted and the back is weakly inverted, and vice versa. These asymptote solutions will serve as initial guess for the final resolution (Expressions 13 to 20 respectively).

For the sake of writing our analytical expressions in close form, we define the following parameters: $K_1 = C_{si}/C_{ox}$, $K_2 = C_{si}/C_{box}$, $G_1 = \frac{q}{C_{ox}} A_{2d}$, $G_2 = \frac{q}{C_{box}} A_{2d}$, $\alpha_1 = (1 + G_1 + K_1)$, $\alpha_2 = (1 + G_2 + K_2)$, index 1 & 2 for front and back interface, index wk & sg for weak and strong inversion.

Equations (4-5) become in weak inversion:

$$V_g = V_{fb} + V_{s1} + K_1.(V_{s1} - V_{s2}) \quad (9)$$

$$V_b = V_{fb} + V_{s2} + K_2.(V_{s2} - V_{s1}) \quad (10)$$

And in strong:

$$V_g = V_{fb} + V_{s1} + G_1.(V_{s1} - V_0) + K_1.(V_{s1} - V_{s2}) \quad (11)$$

$$V_b = V_{fb} + V_{s2} + G_2.(V_{s2} - V_0) + K_2.(V_{s2} - V_{s1}) \quad (12)$$

Using equations 9-10, both interfaces are in weak inversion, surface potential become:

$$V_{s1\_1wk\_2wk} = \frac{(1+K_2).Vg + K_1.V_b}{(1+K_1).(1+K_2) - K_1.K_2} \quad (13)$$

$$V_{s2\_1wk\_2wk} = \frac{(1+K_1).V_b + K_2.Vg}{(1+K_1).(1+K_2) - K_1.K_2} \quad (14)$$

Using equations 11-12, both interfaces are in strong inversion, surface potential become:

$$V_{s1\_1sg\_2sg} = \frac{\alpha_2.Vg + K_1.V_b + G_2.K_1.V0}{G_1.(1+K_1) + K_1 + K_2 + 1} \quad (15)$$

$$V_{s2\_1sg\_2sg} = \frac{\alpha_1.Vb + K_2.Vg + G_1.K_2.V0}{G_1.(1+K_2) + K_1 + K_2 + 1} \quad (16)$$

Using equations 10-11, front interface is in strong inversion and back interface in weak inversion:

$$V_{s1\_1sg\_2wk} = \frac{(1+K_2).Vg + K_1.Vb + G_1.(1+K_2).V0}{G_1.(1+K_2) + K_1 + K_2 + 1} \quad (17)$$

$$V_{s2\_1sg\_2wk} = \frac{\alpha_1.Vb + K_2.Vg + G_1.K_2.V0}{G_1.(1+K_2) + K_1 + K_2 + 1} \quad (18)$$

Using equations 9-12, front interface is in strong inversion and back interface in weak inversion:

$$V_{s1\_1wk\_2sg} = \frac{\alpha_2.Vg + K_1.Vb + G_2.K_1.V0}{G_2.(1+K_1) + K_1 + K_2 + 1} \quad (19)$$

$$V_{s2\_1wk\_2sg} = \frac{(1+K_1).Vb + K_2.Vg + G_2.(1+K_1).V0}{G_2.(1+K_1) + K_1 + K_2 + 1} \quad (20)$$

The final initial guess for both surface potentials (named hereafter as $V_{s1}^0$ and $V_{s2}^0$ ) will be defined as the minimum value derived from the four previous expressions (13 with $V_{s1\_1wk\_2wk}$, 15 with $V_{s1\_1sg\_2sg}$, 17 with $V_{s1\_1sg\_2wk}$, 19 with $V_{s1\_1wk\_2sg}$ for $V_{s1}^0$ and similarly with equations 14, 16, 18, 20 for $V_{s2}^0$), the results are shown in Figures 13 & 14.

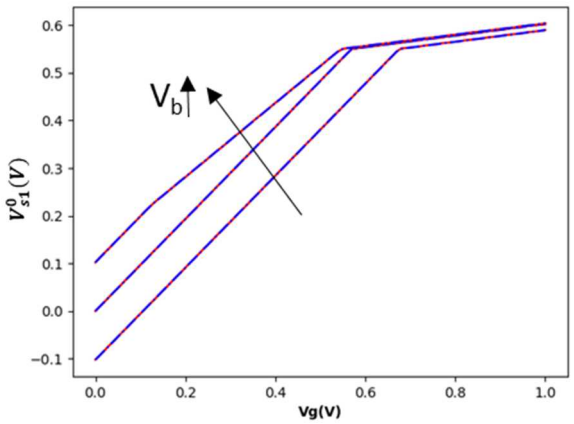


**Fig .13.** Comparison of classical $V_{s1}^0$(Vg) curves as obtained from the numerical model (red solid lines) and the analytical model (blue dashed lines) for various Vb=-3, 0, +3V (T=4K, tox=1nm, tbox=25nm, tsi=10nm).

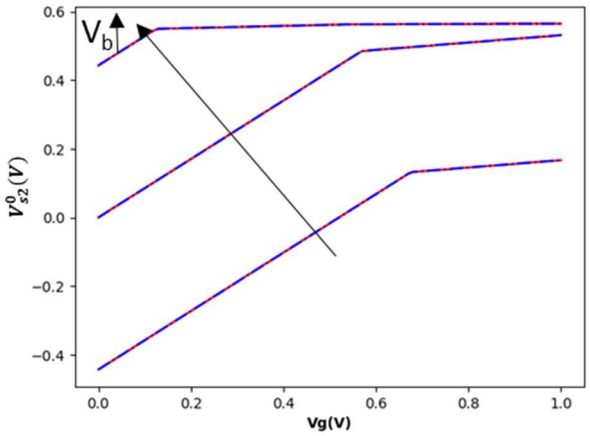


**Fig. 14.** Comparison of classical $V_{s2}^0$(Vg) curves as obtained from the numerical model (red solid lines) and the analytical model (blue dashed lines) for various Vb=-3, 0, +3V (T=4K, tox=1nm, tbox=25nm, tsi=10nm).

Starting from the initial guesses, the final front and back surface potentials are then obtained through a few correction steps, i.e.: $V_{s1,2} = V_{s1,2}^0 + \varepsilon_{1,2}$, where $\varepsilon_{1,2}$ are the computed errors on the front and back surface potentials, respectively.

This correction step has been made using Newton's method. The error expression is derived from the previous system of equations by replacing the term $\frac{q.A_{2d}.k.T}{C_{ox,box}}.F_0\left[\frac{V_{s1,2} - V_0 - \Delta V(F_{1,2})}{kT}\right]$ by its first-order Taylor expansion. Doing so will allow us to have a system of two equations both linear with respect to $\varepsilon_{1,2}$, so that, by solving

this system of equations, we can get to the analytical expressions of $\varepsilon_{1,2}$.

To overcome the numerical problem that occurs only for positive back biases due to the singularity of the Airy subband potential shift near zero electrical field, we introduced a smoothing function in order to avoid any discontinuity for all $V_g$ ranges.

After five corrections, we get a good description of both the front and back surface potentials in all regimes (weak, moderate and strong inversions) as shown in Figs 15 and 16. It should also be noted that a number of smoothing parameters are tuned in order to diminish the numerical problems that could occur in the moderate and strong inversion regions.

Using these exact solutions for the surface potentials, and the $F_0$ Fermi integral function accounting for Fermi-Dirac statistics, we obtain the analytical solution of the inversion charge and compare it to the numerical one (Figure 17).

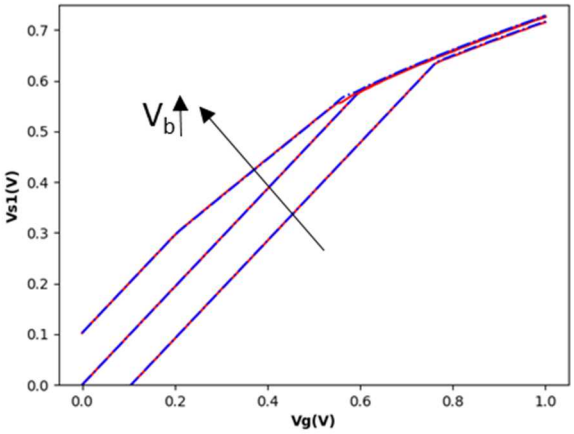


**Fig.15.** Comparison of Vs1(Vg) curves as obtained from the numerical model (red solid lines) and the analytical model (blue dashed lines) for various Vb=-3, 0, +3V (T=4K, tox=1nm, tbox=25nm, tsi=10nm).

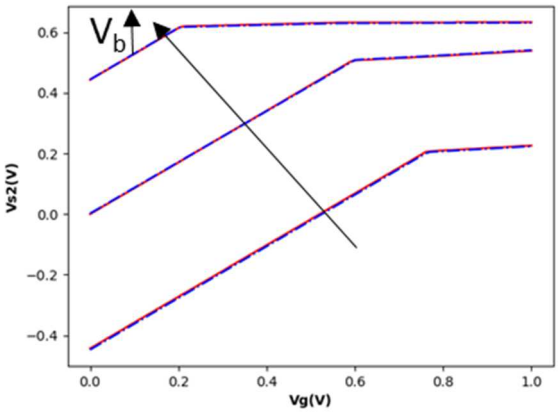


**Fig.16.** Comparison of Vs2(Vg) curves as obtained from the numerical model (red solid lines) and the analytical model (blue dashed lines) for various Vb=-3, 0, +3V (T=4K, tox=1nm, tbox=25nm, tsi=10nm).

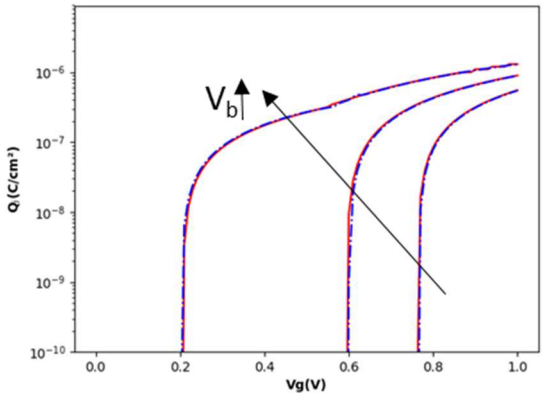


**Fig. 17.** Qi(Vg) curves obtained from the numerical model (red solid lines) and the analytical model (blue dashed lines) for various Vb=-3, 0, +3V (T=4K, tox=1nm, tbox=25nm, tsi=10nm).

## *Conclusions*

In this paper, we have demonstrated for the first time Poisson-Schrödinger simulations and an analytical charge model for a back biased FDSOI structure operated at deep cryogenic temperatures. Moreover, metallic statistics applies around the 0K limit, by replacing the $F_0$ Fermi integral by a Heaviside function. A set of two coupled numerical equations has been established based on a single subband scheme within an Airy's function approach, providing a good description of front/back surface potentials, inversion charges and the gate to channel capacitance of FDSOI structures operated at very low temperature. In order to obtain the analytical solution of the two coupled equations, a classical solution based on the asymptotes in weak and strong inversions, followed by five steps of error correction has been required to converge to the numerical solution. This work is a first step towards a compact model for FDSOI MOSFET that can be used to design circuits in the aim of controlling and reading the Qubits.

## *Acknowledgements*

This work was partially supported by EU ERC synergy project Qucube and EU H2020 RIA project SEQUENCE under grant number 871764.

## *References*

[1] F. Balestra and G. Ghibaudo, “Device and circuit cryogenic operation for low temperature electronics”, Kluwer (2001).

[2] J.M. Hornibrook, et al. “Cryogenic control architecture for large-scale quantum computing”, Physical Review (A), 3.2 024010 (2015).

[3] F. Stern and W.E. Howard, “Properties of semiconductor surface inversion layers in the electric quantum limit”, Physical Review, 163, 816 (1967).

[4] T. Ando, A. B. Fowler, and F. Stern, “Electronic properties of two-dimensional systems”, Rev. Mod. Phys. 54,437–672 (1982).

[5] D. Esseni et al. “An experimental study of mobility enhancement in ultrathin SOI transistors operated in double-gate mode.” IEEE Transactions on Electron Devices 50.3 (2003).

[6] T. Ouisse, “Self-consistent quantum-mechanical calculations in ultrathin silicon-on-insulator structures”, JAP, 76, 5989 (1994).

[7] J.P. Colinge, et al. “Quantum-mechanical effects in trigate SOI MOSFETs”, IEEE TED, 53, 1131 (2006).

[8] T. Poiroux, et al. “Leti-UTSOI2. 1: A Compact Model for UTBB-FDSOI Technologies—Part II: DC and AC Model Description”, IEEE TED, 62, 2760 (2015).

[9] B. Cardoso Paz et al. “Electrostatics and channel coupling on 28nm FDSOI for cryogenic applications”, submitted to ULIS-EUROSOI (2020).

[10] A. P. Gnädinger and H .E. Talley, “Quantum mechanical calculation of the carrier distribution and the thickness of the inversion layer of a MOS field-effect transistor”, SSE, 13, 1301 (1970).

[11] J. Brews, “A charge-sheet model of the MOSFET”, Solid State Electron, 21 (2), pp. 345-355 (1978).

[12] A. Beckers et al “Characterization and modeling of 28 nm bulk CMOS technology down to 4.2 K”. IEEE J Electron Devices Soc 2018.